iScience

CellPress
OPEN ACCESS

Article

Best thermoelectric efficiency of ever-explored materials

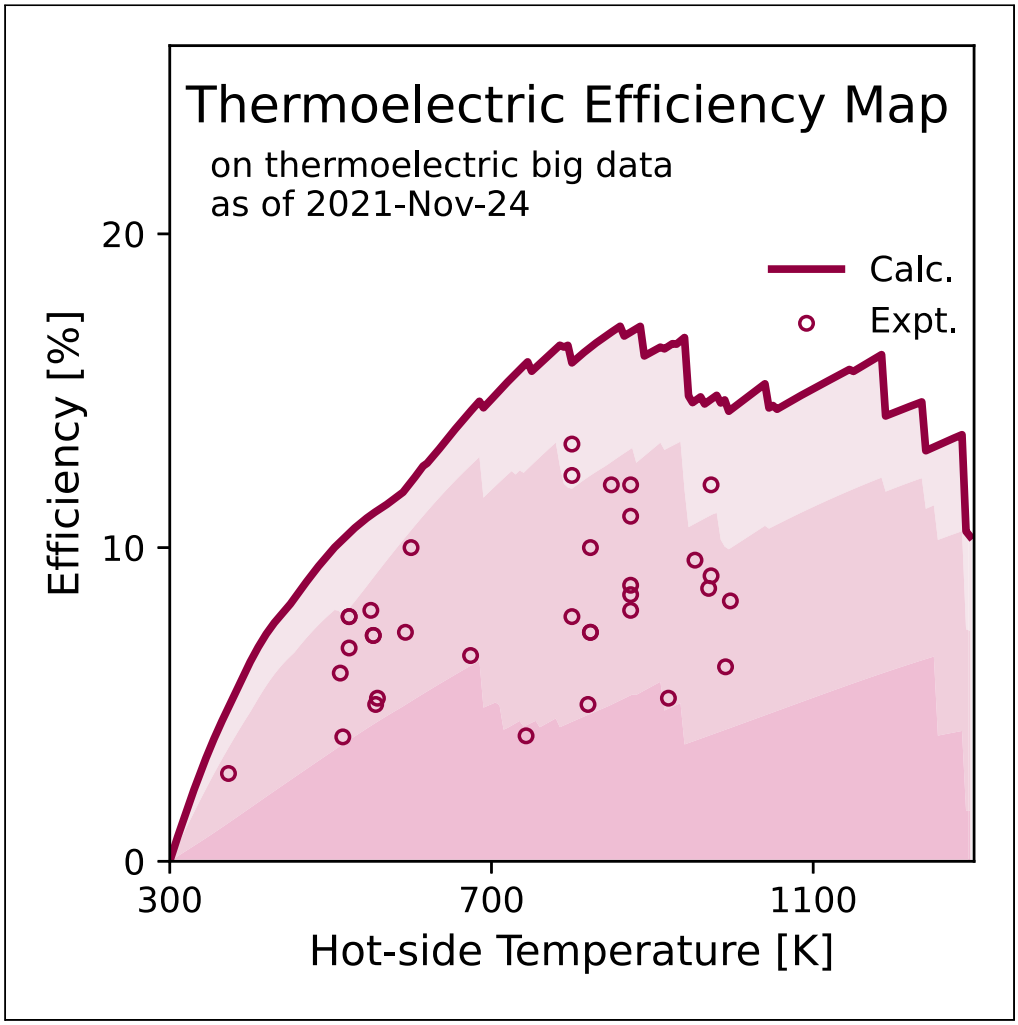

Byungki Ryu, Jaywan Chung, Masaya Kumagai, ..., Yoji Imai, Yukari Katsura, SuDong Park

byungkiryu@keri.re.kr

Highlights

Report of best thermoelectric efficiency of ever-explored materials using big data

100 million device efficiencies calculated over 13 thousand materials

Best single-stage efficiency can reach 17.1%, surpassing 13.3% record

Multistage devices show potential for over 25% efficiency

Ryu et al., iScience 26, 106494
April 21, 2023
https://doi.org/10.1016/j.isci.2023.106494

iScience

CellPress
OPEN ACCESS

Article

Best thermoelectric efficiency of ever-explored materials

Byungki Ryu,[1,5,*] Jaywan Chung,[1] Masaya Kumagai,[2,3] Tomoya Mato,[4] Yuki Ando,[4] Sakiko Gunji,[4] Atsumi Tanaka,[4] Dewi Yana,[4] Masayuki Fujimoto,[4] Yoji Imai,[4] Yukari Katsura,[2,4] and SuDong Park[1]

SUMMARY

A thermoelectric device is a heat engine that directly converts heat into electricity. Many materials with a high figure of merit ZT have been discovered in the anticipation of a high thermoelectric efficiency. However, there has been a lack of investigations on efficiency-based material evaluation, and little is known about the achievable limit of thermoelectric efficiency. Here, we report the highest thermoelectric efficiency using 12,645 published materials. The 97,841,810 thermoelectric efficiencies are calculated using 808,610 device configurations under various heat-source temperatures (T_h) when the cold-side temperature is 300 K, solving one-dimensional thermoelectric integral equations with temperature-dependent thermoelectric properties. For infinite-cascade devices, a thermoelectric efficiency larger than 33% ($\approx {}^1/_3$) is achievable when T_h exceeds 1400 K. For single-stage devices, the best efficiency of 17.1% ($\approx$1/6) is possible when T_h is 860 K. Leg segmentation can overcome this limit, delivering a very high efficiency of 24% ($\approx$1/4) when T_h is 1100 K.

INTRODUCTION

A thermoelectric device composed of P- and N-type thermoelectric material legs placed between hot- and cold-side substrates can directly convert thermal energy into electrical energy via thermoelectric effects.[1,2] As thermoelectric devices can generate electricity regardless of the amount of the temperature difference and heat sources, the thermoelectric technology has been considered a promising solution for power sources in space and waste heat recovery systems in the industry and transportation sectors.[1–7]

One of the most successful applications of thermoelectric technology has been in space exploration, where it has been used in Radioisotope Thermoelectric Generators (RTGs) to generate over a 100 W scale power.[2] Currently, the technology is being investigated for use in industrial and transportation sectors. Commercially available devices are based on Bi_2Te_3 alloys, and each device produces nearly 10 W with a conversion efficiency of approximately 5–7% under a temperature difference of 200–250 K.[3] Using these devices, KELK reported a kW-scale power generation from waste heat in steel works.[3] Additionally, flexible and organic thermoelectrics have been proposed for room temperature energy harvesting and power generation from human body heat, with the potential of producing energy in the order of μW to mW from a temperature difference of approximately 10 K.[6,7]

To put thermoelectric technology into wide and practical use, it is essential to increase the efficiency (η) of the devices. Because a thermoelectric device is a heat engine, the thermoelectric efficiency increases with temperature difference and is bounded by the Carnot efficiency. Moreover, as discovered by Ioffe in 1957,[8] in some cases, the efficiency is determined by a single material parameter, called the dimensionless thermoelectric material figure of merit $ZT = \alpha^2 T/\rho\kappa$, which is defined as the ratio between absolute temperature T and three thermoelectric transport properties (TEPs), namely, the Seebeck coefficient α, electrical resistivity ρ, and thermal conductivity κ. Precisely, for an ideal one-dimensional thermoelectric leg having *temperature-independent* TEPs, the maximum efficiency of thermoelectric conversion (η_{max}) under a given operating temperature range from the cold-side temperature T_c to the heat-source temperature T_h is exactly determined by ZT:

$$\eta_{max} = \frac{T_h - T_c}{T_h} \frac{\sqrt{1+ZT_m} - 1}{\sqrt{1+ZT_m} + T_c/T_h}, \qquad \text{(Equation 1)}$$

[1]Energy Conversion Research Center, Korea Electrotechnology Research Institute (KERI), Changwon 51543, Republic of Korea

[2]Center for Advanced Intelligence Project, RIKEN, Tokyo 103-0027, Japan

[3]SAKURA Internet Research Center, SAKURA internet Inc., Osaka 530-0001, Japan

[4]Research and Services Division of Materials Data and Integrated System (MaDIS), National Institute for Materials Science (NIMS), Ibaraki 305-0044, Japan

[5]Lead contact

*Correspondence: byungkiryu@keri.re.kr

https://doi.org/10.1016/j.isci.2023.106494

where T_m is $(T_h + T_c)/2$. From the observation that the higher the Z, the higher the efficiency, many high ZT materials have been discovered and developed, from the traditional Bi_2Te_3-, PbTe-, GeTe-, and $Si_{1-x}Ge_x$-based alloys[9–12] to the recently developed SnSe- and Mg_3Sb_2-based alloys.[13,14]

However, little is known about the current status of device efficiency. The efficiency estimation using ZT is not very accurate for wide-temperature-range applications because TEPs are *temperature-dependent*.[15,16] Additionally, the estimation ignores several factors introduced in device fabrication processes such as parasitic resistances. Although the measurement of device efficiency is demanded, the number of such experimental studies is less than a few dozen,[11] likely because of more complex processes in device fabrication than in materials synthesis. Therefore, the efficiency-based evaluation of materials and devices is crucial for understanding the current status. Furthermore, determining the achievable limit will guide future directions and accelerate research regarding the design of high-performance devices.

RESULTS

Thermoelectric efficiency exploration

Here, we report the theoretical best thermoelectric efficiency of devices resulting from the ever-explored thermoelectric material data collected in the **Starrydata2.org** thermoelectric database (DB). **Starrydata2** is the world's largest thermoelectric property DB, which contains 43,601 material samples for thermoelectric properties from 7,994 publications as of 2021-November-24.[17] After data filtering, we obtain high-quality thermoelectric *big data* composed of 13,338 samples from 3,120 publications. Then, the material samples in the big data DB are theoretically evaluated by the computed maximum thermoelectric conversion efficiency under various temperature differences of $\Delta T = T_h - T_c$ when $T_c = 300$ K (12,645 samples from 2,919 publications are available for $T > 300$ K): see STAR Methods (data preparation, filtering, and cleansing, thermoelectric device model, and thermoelectric performance calculation). The thermoelectric efficiency is computed by solving one-dimensional thermoelectric integral equations for the temperature distribution $T(x)$ and heat currents at the hot and cold sides[15,16]: see STAR Methods (temperature distribution inside a leg). Using the searched high-performance P- and N-leg samples, of which the efficiency is larger than or equal to 85% of best P- and N-material efficiencies for a given heat source temperature, single-stage P-N leg-pair devices with various leg geometries and interfacial resistances are constructed: see STAR Methods (thermoelectric device model and computation of the best efficiency). The interfacial resistances allow us to include efficiency loss from device fabrication. Finally, the best thermoelectric efficiency for various electrical and thermal operating conditions is theoretically explored over 7,650,225 material efficiency data and 97,841,810 device efficiency data points; overall, 105,492,035 efficiency data spaces are explored; see STAR Methods (computation of the best efficiency).

Best thermoelectric efficiency

Figure 1 shows the achievable best thermoelectric device efficiency ($\eta^{(\mathrm{dev})}$) among 97,841,810 device efficiency data from 808,610 P-N leg-pair thermoelectric device configurations made of 12,645 ever-explored materials, for a given heat-source temperature T_h and fixed $T_c = 300$ K. The infinite-cascade device, where the electric current at each temperature point is optimised, attains the theoretical maximum efficiency for a given ZT curve. We obtain the maximally achievable ZT curve ($ZT_{\mathrm{best}}(T)$) from the DB (see key resources table (**data500**). Hence, the best efficiency of the infinite-cascade device ($\eta_{\max}^{(\infty-\mathrm{Cascade})}$) is simply calculated[18] by

$$\eta_{\max}^{(\infty-\mathrm{Cascade})} = 1 - \exp\left(- \int_{T_c}^{T_h} \frac{dT}{T} \frac{\sqrt{1+ZT_{\mathrm{best}}(T)} - 1}{\sqrt{1+ZT_{\mathrm{best}}(T)} + 1} \right), \qquad \text{(Equation 2)}$$

which increased strictly with T_h. The theoretical maximum efficiency is 25% ($\approx 1/4$) at $T_h = 880$ K ($\Delta T = 580$ K). This high efficiency corresponds to a device ZT value of 2. Furthermore, an even higher theoretical maximum efficiency of 33% ($\approx {}^1/_3$) is possible at $T_h = 1400$ K ($\Delta T = 1100$ K). For single-stage P-N leg devices, the best efficiency increases with T_h and has the highest value of 17.1% ($\approx 1/6$) at $T_h = 860$ K ($\Delta T = 560$ K). However, the best efficiency no longer increases but significantly drops when $T_h > 940$ K. This efficiency drop at very high temperatures is due to the absence of a stable material at high temperatures and material self-compatibility issues[18] arising from the strong temperature dependence of thermoelectric properties and low average ZT. If the radiation and convection losses are considered, the decrease in efficiency at high temperatures will be more significant.[19]

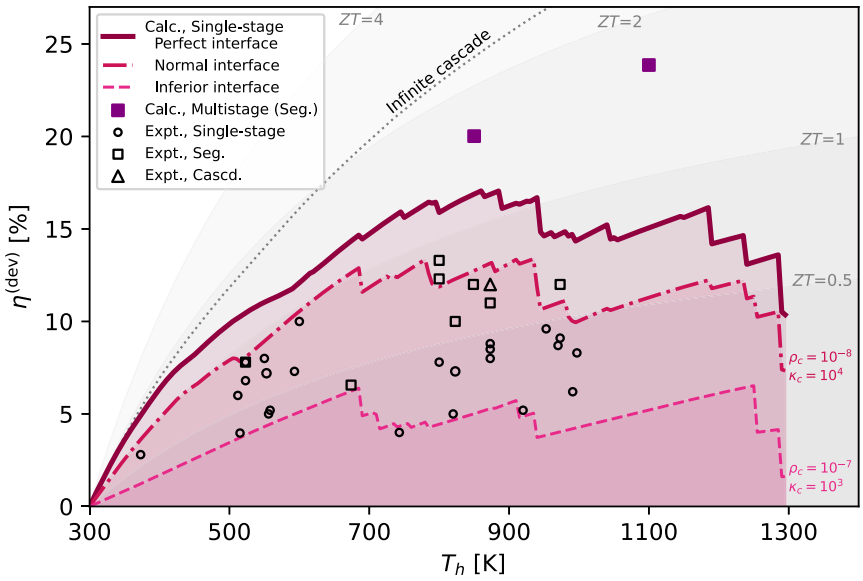

Figure 1. Best thermoelectric efficiency

Thermoelectric efficiencies are explored using the thermoelectric property big data from **Starrydata2** thermoelectric database. After data filtering, 12,645 materials that can be used for power generation above 300 K, are obtained from 2,919 publications. Using high-performance P- and N-leg materials, 808,610 single-stage P-N leg-pair devices were constructed. Then, 97,841,810 device efficiencies were computed over various heat source temperature, electrical currents, geometries, and interfacial resistances, when T_c = 300 K. Finally, best thermoelectric device efficiency is theoretically explored at every heat source temperature. For the clarity, we have only showed the achievable theoretical boundaries for device efficiencies. Solid, dotted-dashed, and dashed lines are the best efficiency curves for single-stage devices with a perfect interface (no thermal and electrical resistances), a normal interface ($\rho_c^{(normal)} = 10^{-8}\ \Omega\ m^2$ and $\kappa_c^{(normal)} = 10^4\ W\ m^{-2}\ K^{-1}$), and an inferior interface ($\rho_c^{(inferior)} = 10^{-7}\ \Omega\ m^2$ and $\kappa_c^{(inferior)} = 10^3\ W\ m^{-2}\ K^{-1}$), respectively. The dotted line is the best efficiency curve for an infinite-cascade device. Filled squares are efficiencies for calculated (Calc.) multistage segmented P-N leg-pair devices working at T_h = 850 K and T_h = 1100 K. Additional data points represent the experimental (Expt.) efficiencies of fabricated devices: single-stage devices (unfilled black circle),[3,20–38] segmented devices (Seg., unfilled black square),[11,22,29,39–43] and a cascaded device (Cascd., unfilled black triangle).[20] The ZT values of the grey-guide lines are inversely calculated using the maximum efficiency Equation 1 for a given T_h when T_c = 300 K: $ZT = \left(\frac{T_h - T_c(1-\eta)}{T_h(1-\eta) - T_c}\right)^2 - 1$.[44] See also key resources table (**data500**) for the best efficiency curves and experimental reports, key resources table (**data300**) for the considered P-N leg-pair configurations, and key resources table (**data400**) for the 100 million P-N leg-pair device efficiencies data.

A multistage structure in devices such as segmented legs may overcome the self-compatibility issue, as theoretically reported by Ouyang and Li in 2016 (η = 21.0% at ΔT = 700 K).[19] Higher theoretical efficiencies have been reported in P-type single-leg device: Ryu et al. in 2021 (η = 21.9–24.5% at ΔT = 600–800 K)[15] and Wabi et al. in 2022 (η = 22.0% at ΔT = 600 K).[45] In addition, in this study, we find a multiple-stage P-N leg pair device with very high efficiency: η = 20.0–23.9% at ΔT = 550–800 K; see key resources table (**data700**) for the device configuration generated.

However, it should be noted that there is a large difference between the theoretical and measured best efficiencies; see Figure 1 and Table 1. For the single-stage devices in Table 1, the measured best efficiencies range from approximately 7–10%: the single-stage Bi_2Te_3-based device by KELK (7.2% at T_h = 553 K)[3] and the GeTe(P)-Mg_3Sb_2(N)-based device by Tongji University (10.0% at T_h = 600 K).[46] For the multistage devices in Table 1, the measured best efficiencies are approximately 12–13%: the GeTe/BiTe(P)-PbSe/Bi_2Te_3(N) segmented device by SUSTECH (13.3% at T_h = 873 K),[11] the half-Heusler (HH)/Bi_2Te_3 segmented device by PSU (12.0% at T_h = 873 K),[39] the skutterudite (SKD)/BiTe segmented device by SICCAS (12.0% at T_h = 849 K),[40] and the PbTe/Bi_2Te_3 cascaded device by AIST (12.0% at T_h = 873 K).[20] However, their efficiency values are much lower than the theoretically best device efficiency of 17.1% found in this work. Such a loss in efficiency may be due to a suboptimal choice of materials and significant interfacial resistances. Thermal radiation and convection might also cause a nonnegligible loss in efficiency when T_h is high.[19]

Table 1. Selected values of the best thermoelectric efficiency (η)

	Device	T_h [K]	T_c [K]	ΔT [K]	η	η_{Carnot}	η_{TE}	Reference
Calc.	Infinite cascade	1400	300	1100	33.0% ≈1/3	78.6%	42.0%	This work
	Segmented (P-N)	1100	300	800	23.9% ≈1/4	72.7%	32.8%	This work
	Single-stage (P-N)	860	300	560	17.1% ≈1/6	65.1%	26.2%	This work
Expt.	Segmented (P-N)	800	294	506	13.3% ≈1/8	63.3%	21.0%	Ref.[11]
	Single-stage (P-N)	600	280	320	10.0% ≈1/10	53.3%	18.8%	Ref.[46]
		553	303	250	7.2% ≈1/14	45.2%	15.9%	Ref.[3]

The efficiencies of multistage and single-stage thermoelectric devices are described with working temperatures, Carnot efficiency ($\eta_{Carnot} = \Delta T/T_h$), and reduced thermoelectric efficiency ($\eta_{TE} = \eta_{Carnot}/\eta$). See also Figure 1 and key resources table (**data500**).

Distribution of thermoelectric properties

Figure 2 shows the distribution of thermoelectric property values in the *filtered* thermoelectric big data of 13,338 published material samples. Figure 2A shows the available temperature ranges that are defined as the range from the minimum measured temperature to the maximum measured temperature for a given material's thermoelectric property. There are two distinct measurement patterns: (1) cryogenic-type thermoelectric property measurements below room temperature (<300 K) and (2) power generation-type measurements above room temperature (>300 K). For the latter, 80% of the samples are measured from 300 K up to 800 K, which are suitable for mid-temperature thermoelectric power generation applications. The highest measured temperature is 1500 K. Figure 2B shows the distribution of 215,526 Seebeck coefficient values ($\alpha(T)$). The distribution is somewhat symmetric between the P- and N-type materials. When $\alpha(T)$ is small, it increases with T, showing metallic behavior. When $\alpha(T)$ is large, it increases with T, while $T < 300$ K, showing bipolar transport behavior of the narrow-gap semiconductors. Figure 2C shows the distribution of 223,404 electric resistivity values. The resistivity varies exponentially with temperature. For temperatures below 300 K, most of the explored samples have very small resistivity, similar to semimetallic or heavily doped semiconductors. Some have very high resistivity, which might be related to charge carrier quenching in doped semiconductors. For temperatures larger than 300 K, the distribution is symmetrical about the axis of the critical value $\rho_{crit} = 10^{-4}\ \Omega$ m. Furthermore, the resistivity value seems to converge to ρ_{crit} as the temperature increases. Figure 2D shows the distribution of the 187,244 thermal conductivity values. When the temperature is below 100 K, there are unusually small and large lattice thermal conductivities. The small value is due to the small number of phonon activation modes, while the large value is due to less phonon scattering and ballistic phonon transport. With increasing temperature, the number of large thermal conductivity samples decreases, which may be due to the activation of the Umklapp three-phonon process. On the whole, the samples can have small thermal conductivities below 10 W m^{-1} K^{-1} above 300 K.

History of thermoelectric performances: ZT and efficiency

For decades, the thermoelectric performance of materials has been developed to search for high ZT values. Figure 3A shows how the best ZT value has been improved over time. In 2000, the ZT exceeded 1 for the first time due to nanostructuring and low thermal conductivity.[47,48] Then, the ZT finally reached 2 due to the synergetic effect of electron and phonon transport[10,49]; the largest improvement was achieved in the mid-temperature range of approximately 600–950 K. Recent studies report very high peak ZT values exceeding 2.5 in GeTe[11] and SnSe.[13]

Figure 3B shows how the best thermoelectric material efficiency ($\eta^{(mat)}$) of single-leg P- or N-type materials has been improved over time for various T_h's and $T_c = 300$ K. Between 2000 and 2009, the material efficiency was highly enhanced for all temperature ranges, similar to the improvement of ZT values. The

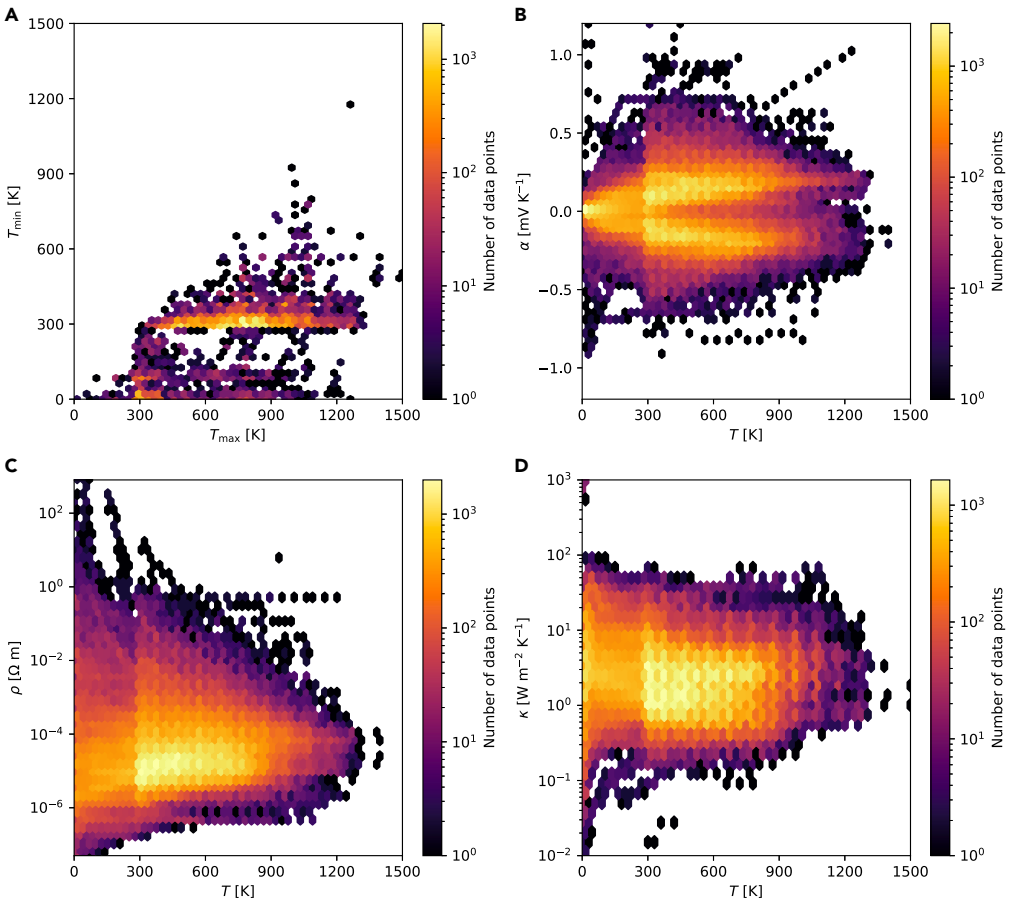

Figure 2. Distribution of thermoelectric properties

(A–D) (A) Hexa-bin plot of the maximum and minimum available temperatures from the samples' thermoelectric properties. Hexa-bin plots of the (B) Seebeck coefficient distribution, (C) electrical resistivity distribution, and (D) thermal conductivity distribution over measured temperatures. In each panel, color represents the number of data points. Note that **Starrydata2** contains 43,601 material samples for thermoelectric properties from 7,994 publications as of 2021-November-24. After data filtering, high-quality thermoelectric big data composed of 13,338 samples from 3,120 publications is obtained and displaced. See also key resources table (**data010**) and STAR Methods (data preparation, filtering, and cleansing).

improvement was the largest at $T_h \approx 900$ K, similar to the improvement of the peak ZT. However, after 2010, the increase in the best efficiency for low- and high-temperature applications has been rather small. This is mainly because, even if the peak ZT is high, the average ZT can be low. Additionally, for wide-temperature applications, the self-compatibility problem[18] of materials may also responsible for the limited efficiency increase. Our observation of the large discrepancy between ZT and the material efficiency implies the importance of studying device efficiency.

Performance by material composition

Figure 4 shows the ideal thermoelectric material efficiency over 17 material groups based on material composition; see the key resources table (**data150** and **data261**). In Figure 4A, the theoretical material performances are represented for well-known telluride alloys (Te-alloys): Bi_2Te_3-, $AgSbTe_2$-, GeTe-, and (Pb,Sn)Te-based alloys. For Te alloys, P-type materials perform better than N-type materials. Bi_2Te_3 alloys are the best materials for low-temperature heat sources ($T_h < 600$ K); their best efficiency can reach 10–12%. For mid-temperature heat sources (600 K < T_h < 950 K), P-type $AgSbTe_2$-, GeTe-, and (Pb,Sn)Te-based alloys show superior thermoelectric conversion performance compared to other alloys.

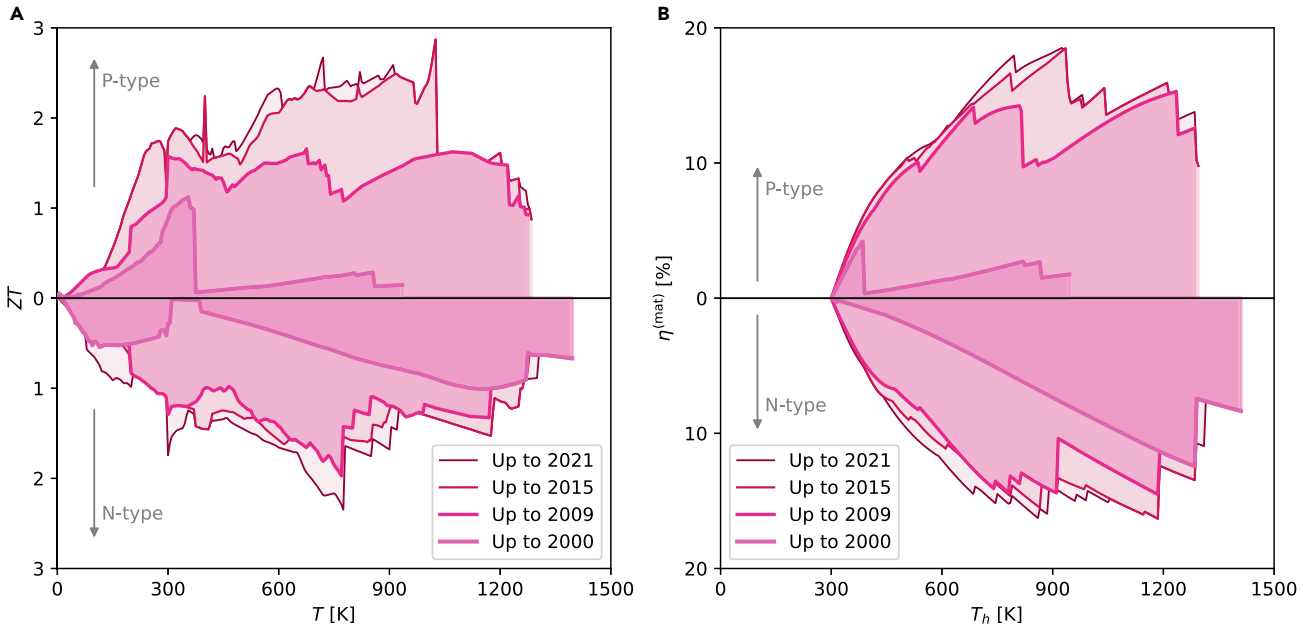

Figure 3. History of thermoelectric performances: *ZT* and efficiency

(A and B) (A) The best material figure of merit *ZT* and (B) best thermoelectric material efficiency $\eta^{(mat)}$ for the given year ranges were drawn over ever-explored materials. The achievable best *ZT* and $\eta^{(mat)}$ were explored over 13,338 samples from 3,120 publications (see also key resources table (**data070**)) and 12,645 samples from 2,919 publications (see also key resources table (**data261**)), respectively. Note that the number of samples for the latter is smaller than the former owing to the temperature range restriction: $T > 300$ K for efficiency calculations.

In Figure 4B, the thermoelectric material performances of oxide-, sulfide-, and selenide-related alloys (X-O, X-S, X-Se) are provided. Compared to tellurides, these alloys can operate at high temperatures. In the case of La_2S_3, although ΔT is very large (1100 K), its best material efficiency is smaller than that of Bi_2Te_3 for ΔT = 300 K. In Figure 4C, the performances of Mg and Si alloys are shown. Note that the P-type MgAgSb-based and N-type Mg_3Sb_2-based materials have comparable efficiency to Bi_2Te_3-based devices for low-temperature heat sources, which explains the experimental device efficiency.[21] For N-type materials, Mg_2Si-based alloys exhibit good thermoelectric performance at mid-temperatures. Alternatively, $Si_{1-x}Ge_x$ alloys demonstrate good performance at high temperatures ($T_h > 950$ K), as reported.[12] Figure 4D shows high-temperature thermoelectric materials such as clathrate (Clath.), HH, and SKD thermoelectric materials and other antimonide compounds (X-Sb). Although their performance is relatively poor at low and mid-temperatures, they show the best efficiency with regard to high-temperature heat sources.

Representative P-N leg-pair devices

Figure 5 and Table 2 show the theoretical device efficiency curves of nine representative single-stage P-N leg-pair devices; see key resources table (**data400** and **data600**). Within available temperature ranges, the device efficiencies increase with temperature, indicating that thermoelectric efficiencies are limited by the available temperature ranges, which might be determined by the material thermal stability. For low-temperature heat sources, the fully Bi_2Te_3-based P-N leg-pair device shows the best device efficiency, which is higher than 10%. For 600 K < T_h < 950 K, the devices based on P-type chalcogenides and N-type Mg_3Sb_2, Mg_2(Si,Sn), HH, or SKD show the highest efficiency. A limit efficiency of 17% is found in the single-stage PbTe-SKD and SnSe-SKD devices. For $T_h > 950$ K, however, the device efficiency is smaller than that of mid-temperature devices. Notably, there is a distinct pattern in the curves; that is, the curves for low-temperature devices are concave, but the other curves are convex at low temperatures and become linear at high temperatures. The convexity of the curves is related to the poor *ZT* value at low temperatures in addition to the temperature-dependent nature of thermoelectric transport properties. This suggests that the temperature gradient in thermoelectric properties should be controlled using segmented or cascaded device structures. On the other hand, the linearity of the curves at high temperatures implies that linear extrapolation of the curves can be used to estimate the efficiency at higher temperatures.

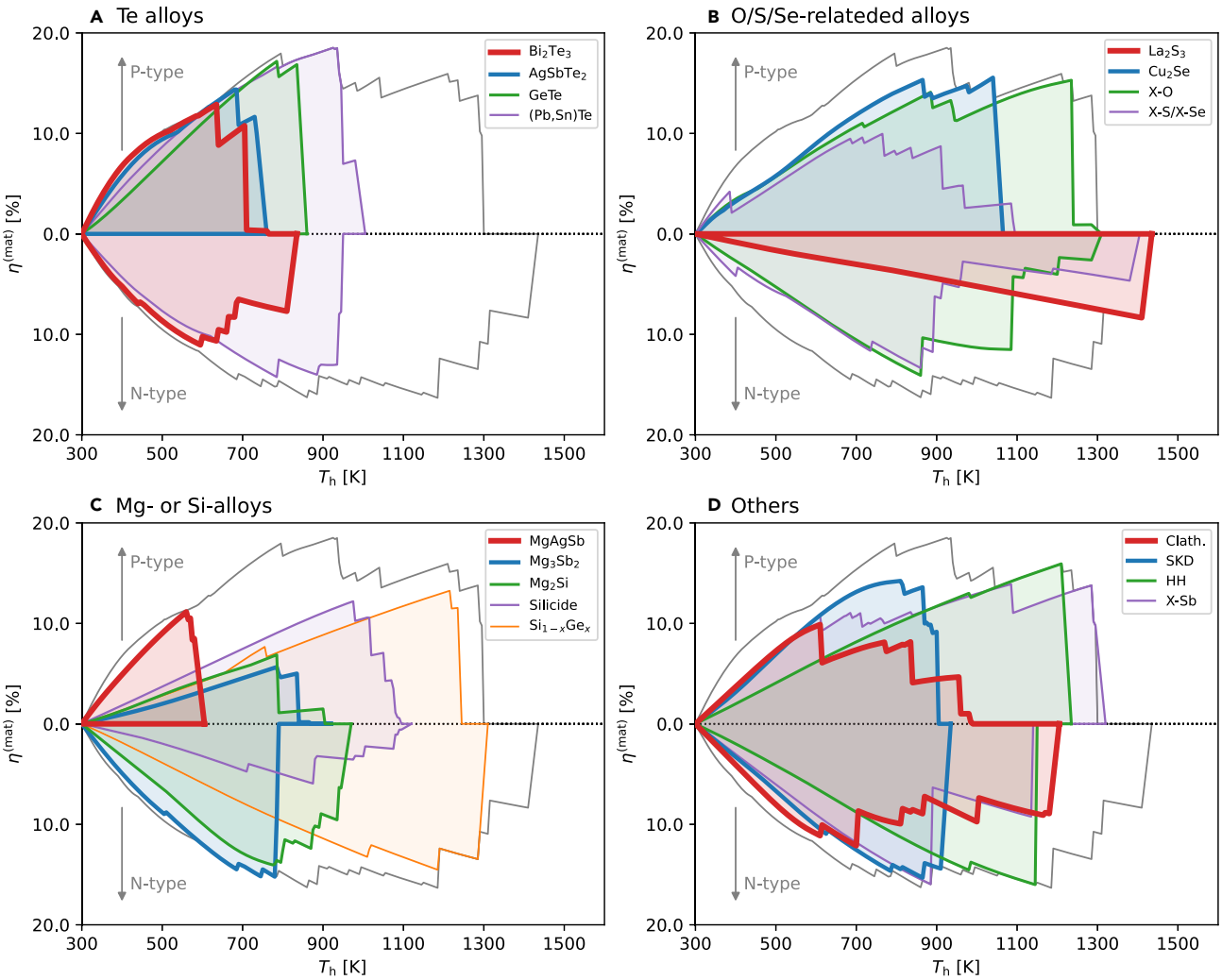

Figure 4. Performance by material composition

(A–D) Achievable thermoelectric material efficiencies for 17 material groups are drawn for (A) Te alloys, (B) O/S/Se-related alloys, (C) Mg- or Si-based alloys, and (D) other alloys. See also key resources table (**data150** and **data261**) and STAR Methods (material group classification of compositions) for sample material group classification.

Efficiency loss due to interfacial resistances

Figure 6 shows the degradation of efficiency of P-N leg-pair devices under electrical and thermal contact resistances compared to the best efficiency of perfect devices; see key resources table (**data500**). While the P and N legs generate electrical power, some of the power is lost via internal resistances.[19] The P- and N-type thermoelectric semiconductors are metallized and connected to the electrodes on the substrates, and the device substrates are in contact with the external heat source and sink. Such a complex layered structure causes parasitic electrical and thermal interfacial resistances (ρ_c and κ_c^{-1}), resulting in net power reduction. The net temperature difference decreases with interfacial thermal resistance, and additional Joule heating occurs at the ends of the legs via additional interfacial electrical resistance. When contact resistances are extremely small ($\rho_c = 10^{-10}\ \Omega\ m^2$ and $\kappa_c = 10^5\ W\ m^{-2}\ K^{-1}$), the relative efficiency loss is only 1.5% less than the best device efficiency with perfect contact. For $\rho_c = 10^{-9}\ \Omega\ m^2$ and $\kappa_c = 10^4\ W\ m^{-2}\ K^{-1}$, the drop in the best efficiency is approximately 12% on average. For the normal interface condition with $\rho_c = 10^{-8}\ \Omega\ m^2$ and $\kappa_c = 10^4\ W\ m^{-2}\ K^{-1}$, the enhanced interfacial Joule heating causes a significant drop in relative efficiency by 22% on average. For an inferior interface condition ($\rho_c = 10^{-7}\ \Omega\ m^2$ and $\kappa_c = 10^3\ W\ m^{-2}\ K^{-1}$), a large efficiency loss occurs (67% loss on average), and the best efficiency is highly reduced to 6.5% ($\approx$1/15).

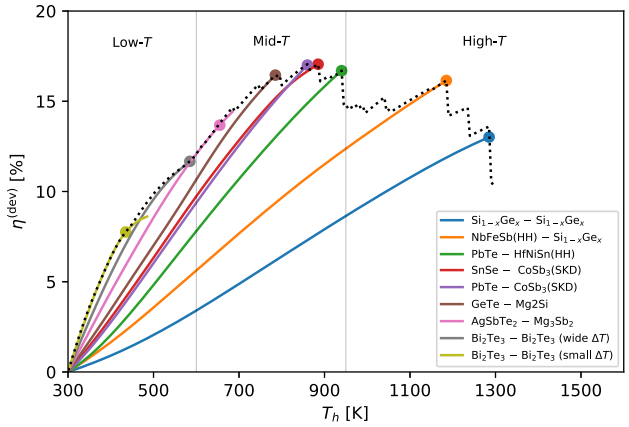

Figure 5. Representative P-N leg-pair devices

Thermoelectric device efficiency curves are drawn for 9 representative devices with respect to various heat-source temperatures when T_c is 300 K. Low-T (T_h < 600 K), mid-T (600 K < T_h < 950 K), and high-T (T_h > 950 K) range applications are separated with vertical gray lines. The dotted line indicates the achievable best device efficiencies using single-stage P-N leg devices. The dot on each curve means that the device has realized the achievable best efficiency. The best efficiency is computed with leg-area ratio optimization. See also Table 2 and the key resources table (**data400** and **data600**) for detailed information on the designed P-N leg-pair devices.

For a given device, the maximum generated power P_{max} can be approximately determined from the generated voltage V_{dev} and total internal resistance R_{dev},[15] as follows:

$$P = I(V_{dev} - IR) \leq P_{max} \cong \frac{V_{dev}^2}{4R_{dev}} = \frac{\overline{\alpha}^2 \Delta T_{eff}}{4(R_{mat} + R_c)}, \quad \text{(Equation 3)}$$

where $\overline{\alpha}$ is the *average* Seebeck coefficient over the effective working temperature difference ΔT_{eff}, R_{mat} is the electrical resistance of thermoelectric material, and R_c is the parasitic interfacial/contact resistance. Thermal interfacial resistance causes a temperature drop at the interface ($\Delta T_{IF} > 0$).[15] In addition, the Peltier heat flow causes higher ΔT_{IF} and lower $\Delta T_{eff} = \Delta T - \Delta T_{IF} < \Delta T_{ideal} = T_h - T_c$, compared to the open-circuit condition.[15,66] As a result, the device power and efficiency can be significantly decreased by the interfacial thermal and electrical resistances.

Table 2. Representative thermoelectric P-N leg-pair devices

P-leg composition (Ref., sample ID)	N-leg composition	T_h [K]	ΔT [K]	$\eta^{(dev)}$	A_p/A_n
$Si_{0.8}Ge_{0.2}$/P (ref.[50], sampleid = 21962)	$Si_{80}Ge_{20}$ (ref.[51], sampleid = 21190)	1285	985	13.02%	0.939
$(Nb_{0.60}Ta_{0.40})_{0.8}Ti_{0.2}FeSb$ (ref.[52], sampleid = 31566)	$Si_{80}Ge_{20}$ (ref.[53], sampleid = 21211)	1185	885	16.15%	0.426
$Pb_{0.9}Na_{0.02}Mg_{0.08}Te$ (ref.[54], sampleid = 300)	$(Hf_{0.6}Zr_{0.4})NiSn_{0.99}Sb_{0.01}$ - $W_{0.087}$ (ref.[55], sampleid = 38585)	940	640	16.70%	3.615
$Sn_{0.97}Na_{0.03}Se_{0.9}S_{0.1}$ (ref.[56], sampleid = 41016)	$Yb_{0.3}Co_4Sb_{14.4}$ (ref.[57], sampleid = 41697)	885	585	17.05%	3.181
$Na_{0.035}Eu_{0.03}Mn_{0.03}Pb_{0.905}Te$ (ref.[58], sampleid = 35891)	$xCo/Ba_{0.3}In_{0.3}Co_4Sb_{12}$, x = 0.2% (ref.[59], sampleid = 31358)	860	560	17.01%	3.391
$Ge_{0.89}Sb_{0.1}In_{0.01}Te$ (ref.[60], sampleid = 31973)	$Mg_2(Si_{0.4}Sn_{0.6})Sb_{0.018}$ (ref.[61], sampleid = 9777)	785	485	16.45%	1.912
$AgSbTe_2$ (ref.[62], sampleid = 16668)	$Mg_{3.15}Mn_{0.05}Sb_{1.5}Bi_{0.49}Se_{0.01}$ (ref.[63], sampleid = 27133)	655	355	13.68%	0.961
$Bi_{0.4}Sb_{1.6}Te_3Ag_{0.003}$ (ref.[64], sampleid = 38722)	$Bi_{0.24}Sb_{0.05}Te_{0.61}Se_{0.10}$ (ref.[30], sampleid = 38264)	585	285	11.67%	1.106
$Bi_{0.5}Sb_{1.5}Te_3$ (ref.[9], sampleid = 42662)	$Y_{0.2}Bi_{1.8}Se_{0.3}Te_{2.7}$ (ref.[65], sampleid = 16900)	435	135	7.75%	1.034

Thermoelectric device efficiencies of nine representative thermoelectric P-N leg-pair devices and corresponding P- and N-leg compositions with sample ID (sampleid) numbers in **Starrydata2**. See Figure 5 and the key resources table (**data400** and **data600**).

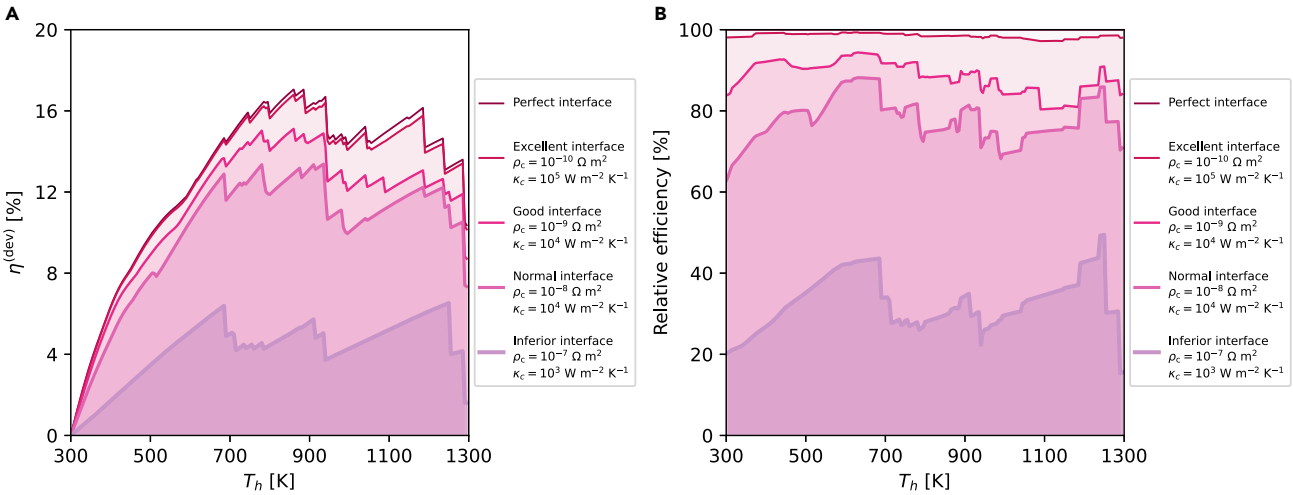

Figure 6. Efficiency loss due to interfacial resistances

(A) The achievable best thermoelectric device efficiency under interfacial electrical and thermal resistances.

(B) Relative efficiency of the best device efficiency under interfacial electrical and thermal resistances compared to the perfect interface devices. See also key resources table (**data500**) for detailed information.

The interfacial thermal resistance between the thermoelectric devices and outside heat source/sink can be characterized using impedance spectroscopy[67] and I-V measurement methods.[66] These methods yielded the thermal contact conductivities of 5,800–19,000 W m^{-2} K^{-1} and 2,800 W m^{-2} K^{-1}, respectively, which are comparable to the good/bad interfaces, as shown in Figure 6. However, the exact interface responsible for the significant increase in resistance has not yet been identified, and could be situated between the materials, electrodes, substrates, or heat sources. A spatially resolved method such as the time-domain thermoreflectance method[68] may play an important role in characterizing the *position-dependent* local thermal conductivity inside a leg and device. On the other hand, the electrical interfacial/contact resistance has been characterized by the spatial resolution measurement of the electrical potential along a single leg.[69] Recently, low contact resistivity of $\rho_c \leq 10^{-9}$ Ω m^2 has been developed in contacted thermoelectric legs for several alloy systems.[70,71] A 14% single-leg $\eta^{(mat)}$ was reportedly achieved for contact-developed GeTe alloys under ΔT = 440 K and T_c = 300 K.[70]

Conclusion

The achievable best thermoelectric device efficiencies are theoretically investigated over ever-explored materials. Theoretically, an efficiency of $^1/_3$ is possible in an infinite-cascade device. An efficiency of 1/4 is possible in a segmented device, while an efficiency of 1/6 is possible in a single-stage device. However, these theoretical limits are much higher than the measured device efficiencies of $^1/_8$ and 1/10 of the multi-stage and single-stage devices. A poor interface quality may yield a low conversion efficiency of 1/15 to 1/14. The discrepancy between theoretical and experimental efficiency can be mitigated in multistage devices by reducing interfacial resistance and selecting optimal thermoelectric materials. It ultimately suggests that collaboration between materials and energy-related fields could accelerate the industrialization of thermoelectric power generation technology.

Limitations of the study

Although the thermoelectric property data from **Starrydata2** are filtered, the thermoelectric property dataset used in this study may contain errors. This study is based on theoretical efficiency calculations using one-dimensional thermoelectric equations, assuming that heat and current follows a one-dimensional path. In addition, the calculations neglect the thermal energy loss by radiation and convection processes. Therefore, the efficiencies in this study are overestimated compared to three-dimensional calculations. Thus, the best efficiency reported in this study is the upper bound of the best thermoelectric efficiency of ever-explored materials.

STAR★METHODS

Detailed methods are provided in the online version of this paper and include the following:

- KEY RESOURCES TABLE
- RESOURCE AVAILABILITY
  - Lead contact
  - Materials availability
  - Data and code availability
- EXPERIMENTAL MODEL AND SUBJECT DETAILS
- METHOD DETAILS
  - Overview of efficiency calculation process
  - Data preparation, filtering, and cleansing
  - Thermoelectric device model
  - Thermoelectric performance calculation
  - Temperature distribution inside a leg
  - Computation of the best efficiency
  - Dimensional effect and radiation loss
  - Material group classification of compositions
- ADDITIONAL RESOURCES

ACKNOWLEDGMENTS

This work was supported by the Korea Electrotechnology Research Institute (KERI) Primary research program through the National Research Council of Science & Technology (NST) funded by the Ministry of Science and ICT (MSIT) (23A01002), by the Korea Institute of Energy Technology Evaluation and Planning (KETEP) grant funded by the Ministry of Trade, Industry and Energy (MOTIE) (2021202080023D), and by the National Research Foundation of Korea (NRF) grant funded by the Korea Government (MSIT) (2022M3C1C8093916), the Republic of Korea. Y.K. and M.K. were supported by the Japan Science and Technology Agency (JST) CREST grant number (JPMJCR19J1), Japan.

AUTHOR CONTRIBUTIONS

B.R. conceptualized the study, led the design of the work, filtered the data, performed the efficiency calculations, analyzed the efficiency data, created the figures, and wrote the article. J.C. developed the software, analyzed the efficiency data, discussed the results, and wrote the article. S.P. supervised the project and discussed the results. M.K. and T.M. developed the Starrydata web system and generated the dataset file. Y.A., S.G., A.T., D.Y., and M.F. collected the thermoelectric property data from publications. S.G., Y.I., A.T., and Y.K. collected target publications. M.K. and Y.K. served as an advisor on the project and discussed the results.

DECLARATION OF INTERESTS

The authors declare no competing interests.

Received: December 15, 2022
Revised: March 14, 2023
Accepted: March 22, 2023
Published: March 27, 2023

REFERENCES

1. Goldsmid, H.J. (2016). Introduction to Thermoelectricity (Springer). https://doi.org/10.1007/978-3-662-49256-7.

2. D.M. Rowe, ed. (2006). Thermoelectrics Handbook: Macro to Nano (CRC/Taylor & Francis).

3. Kuroki, T., Kabeya, K., Makino, K., Kajihara, T., Kaibe, H., Hachiuma, H., Matsuno, H., and Fujibayashi, A. (2014). Thermoelectric generation using waste heat in steel works. J. Electron. Mater. *43*, 2405–2410. https://doi.org/10.1007/s11664-014-3094-5.

4. Beretta, D., Neophytou, N., Hodges, J.M., Kanatzidis, M.G., Narducci, D., Martin-Gonzalez, M., Beekman, M., Balke, B., Cerretti, G., Tremel, W., et al. (2019). Thermoelectrics: from history, a window to the future. Mater. Sci. Eng. R Rep. *138*, 100501. https://doi.org/10.1016/j.mser.2018.09.001.

5. Bu, Z., Zhang, X., Hu, Y., Chen, Z., Lin, S., Li, W., Xiao, C., and Pei, Y. (2022). A record thermoelectric efficiency in tellurium-free modules for low-grade waste heat recovery. Nat. Commun. *13*, 237. https://doi.org/10.1038/s41467-021-27916-y.

6. Bahk, J.-H., Fang, H., Yazawa, K., and Shakouri, A. (2015). Flexible thermoelectric materials and device optimization for wearable energy harvesting. J. Mater. Chem. C *3*, 10362–10374. https://doi.org/10.1039/C5TC01644D.

7. Russ, B., Glaudell, A., Urban, J.J., Chabinyc, M.L., and Segalman, R.A. (2016). Organic

thermoelectric materials for energy harvesting and temperature control. Nat. Rev. Mater. *1*, 16050. https://doi.org/10.1038/natrevmats.2016.50.

8. Ioffe, A.F. (1957). Semiconductor Thermoelements and Thermoelectric Cooling, 1st edition (Infosearch).

9. Kim, S.I., Lee, K.H., Mun, H.A., Kim, H.S., Hwang, S.W., Roh, J.W., Yang, D.J., Shin, W.H., Li, X.S., Lee, Y.H., et al. (2015). Dense dislocation arrays embedded in grain boundaries for high-performance bulk thermoelectrics. Science *348*, 109–114. https://doi.org/10.1126/science.aaa4166.

10. Biswas, K., He, J., Blum, I.D., Wu, C.-I., Hogan, T.P., Seidman, D.N., Dravid, V.P., and Kanatzidis, M.G. (2012). High-performance bulk thermoelectrics with all-scale hierarchical architectures. Nature *489*, 414–418. https://doi.org/10.1038/nature11439.

11. Jiang, B., Wang, W., Liu, S., Wang, Y., Wang, C., Chen, Y., Xie, L., Huang, M., and He, J. (2022). High figure-of-merit and power generation in high-entropy GeTe-based thermoelectrics. Science *377*, 208–213. https://doi.org/10.1126/science.abq5815.

12. Wang, X.W., Lee, H., Lan, Y.C., Zhu, G.H., Joshi, G., Wang, D.Z., Yang, J., Muto, A.J., Tang, M.Y., Klatsky, J., et al. (2008). Enhanced thermoelectric figure of merit in nanostructured n-type silicon germanium bulk alloy. Appl. Phys. Lett. *93*, 193121. https://doi.org/10.1063/1.3027060.

13. Zhou, C., Lee, Y.K., Yu, Y., Byun, S., Luo, Z.-Z., Lee, H., Ge, B., Lee, Y.-L., Chen, X., Lee, J.Y., et al. (2021). Polycrystalline SnSe with a thermoelectric figure of merit greater than the single crystal. Nat. Mater. *20*, 1378–1384. https://doi.org/10.1038/s41563-021-01064-6.

14. Ohno, S., Imasato, K., Anand, S., Tamaki, H., Kang, S.D., Gorai, P., Sato, H.K., Toberer, E.S., Kanno, T., and Snyder, G.J. (2018). Phase boundary mapping to obtain n-type Mg3Sb2-based thermoelectrics. Joule *2*, 141–154. https://doi.org/10.1016/j.joule.2017.11.005.

15. Ryu, B., Chung, J., and Park, S. (2021). Thermoelectric degrees of freedom determining thermoelectric efficiency. iScience *24*, 102934. https://doi.org/10.1016/j.isci.2021.102934.

16. Ryu, B., Chung, J., Choi, E.-A., Ziolkowski, P., Müller, E., and Park, S. (2020). Counterintuitive example on relation between ZT and thermoelectric efficiency. Appl. Phys. Lett. *116*, 193903. https://doi.org/10.1063/5.0003749.

17. Katsura, Y., Kumagai, M., Kodani, T., Kaneshige, M., Ando, Y., Gunji, S., Imai, Y., Ouchi, H., Tobita, K., Kimura, K., and Tsuda, K. (2019). Data-driven analysis of electron relaxation times in PbTe-type thermoelectric materials. Sci. Technol. Adv. Mater. *20*, 511–520. https://doi.org/10.1080/14686996.2019.1603885.

18. Snyder, G.J., and Ursell, T.S. (2003). Thermoelectric efficiency and compatibility. Phys. Rev. Lett. *91*, 148301. https://doi.org/10.1103/PhysRevLett.91.148301.

19. Ouyang, Z., and Li, D. (2016). Modelling of segmented high-performance thermoelectric generators with effects of thermal radiation, electrical and thermal contact resistances. Sci. Rep. *6*, srep24123. https://doi.org/10.1038/srep24123.

20. Jood, P., Ohta, M., Yamamoto, A., and Kanatzidis, M.G. (2018). Excessively doped PbTe with Ge-induced nanostructures enables high-efficiency thermoelectric modules. Joule *2*, 1339–1355. https://doi.org/10.1016/j.joule.2018.04.025.

21. Liu, Z., Sato, N., Gao, W., Yubuta, K., Kawamoto, N., Mitome, M., Kurashima, K., Owada, Y., Nagase, K., Lee, C.-H., et al. (2021). Demonstration of ultrahigh thermoelectric efficiency of ~7.3% in Mg3Sb2/MgAgSb module for low-temperature energy harvesting. Joule *5*, 1196–1208. https://doi.org/10.1016/j.joule.2021.03.017.

22. Hu, X., Jood, P., Ohta, M., Kunii, M., Nagase, K., Nishiate, H., Kanatzidis, M.G., and Yamamoto, A. (2016). Power generation from nanostructured PbTe-based thermoelectrics: comprehensive development from materials to modules. Energy Environ. Sci. *9*, 517–529. https://doi.org/10.1039/C5EE02979A.

23. Poon, S.J., Wu, D., Zhu, S., Xie, W., Tritt, T.M., Thomas, P., and Venkatasubramanian, R. (2011). Half-Heusler phases and nanocomposites as emerging high-ZT thermoelectric materials. J. Mater. Res. *26*, 2795–2802. https://doi.org/10.1557/jmr.2011.329.

24. Yu, J., Xing, Y., Hu, C., Huang, Z., Qiu, Q., Wang, C., Xia, K., Wang, Z., Bai, S., Zhao, X., et al. (2020). Half-Heusler thermoelectric module with high conversion efficiency and high power density. Adv. Energy Mater. *10*, 2000888. https://doi.org/10.1002/aenm.202000888.

25. Geng, H., Ochi, T., Suzuki, S., Kikuchi, M., Ito, S., and Guo, J. (2013). Thermoelectric properties of multifilled skutterudites with La as the main filler. J. Electron. Mater. *42*, 1999–2005. https://doi.org/10.1007/s11664-013-2501-7.

26. Xing, T., Song, Q., Qiu, P., Zhang, Q., Gu, M., Xia, X., Liao, J., Shi, X., and Chen, L. (2021). High efficiency GeTe-based materials and modules for thermoelectric power generation. Energy Environ. Sci. *14*, 995–1003. https://doi.org/10.1039/D0EE02791J.

27. Lu, X., Zhang, Q., Liao, J., Chen, H., Fan, Y., Xing, J., Gu, S., Huang, J., Ma, J., Wang, J., et al. (2020). High-efficiency thermoelectric power generation enabled by homogeneous incorporation of MXene in $(Bi,Sb)_2Te_3$ matrix. Adv. Energy Mater. *10*, 1902986. https://doi.org/10.1002/aenm.201902986.

28. Aoyama, I., Kaibe, H., Rauscher, L., Kanda, T., Mukoujima, M., Sano, S., and Tsuji, T. (2005). Doping effects on thermoelectric properties of higher manganese silicides (HMSs, MnSi1.74) and characterization of thermoelectric generating module using p-type (Al, Ge and Mo)-doped HMSs and n-type Mg2Si0.4Sn0.6 legs. Jpn. J. Appl. Phys. *44*, 4275. https://doi.org/10.1143/JJAP.44.4275.

29. Anatychuk, L.I., Vikhor, L.N., Strutynska, L.T., and Termena, I.S. (2011). Segmented generator modules using Bi2Te3-based materials. J. Electron. Mater. *40*, 957–961. https://doi.org/10.1007/s11664-010-1468-x.

30. Zhu, B., Liu, X., Wang, Q., Qiu, Y., Shu, Z., Guo, Z., Tong, Y., Cui, J., Gu, M., and He, J. (2020). Realizing record high performance in n-type Bi_2Te_3-based thermoelectric materials. Energy Environ. Sci. *13*, 2106–2114. https://doi.org/10.1039/D0EE01349H.

31. Fu, C., Bai, S., Liu, Y., Tang, Y., Chen, L., Zhao, X., and Zhu, T. (2015). Realizing high figure of merit in heavy-band p-type half-Heusler thermoelectric materials. Nat. Commun. *6*, 8144. https://doi.org/10.1038/ncomms9144.

32. Hao, F., Qiu, P., Tang, Y., Bai, S., Xing, T., Chu, H.-S., Zhang, Q., Lu, P., Zhang, T., Ren, D., et al. (2016). High efficiency Bi2Te3-based materials and devices for thermoelectric power generation between 100 and 300 °C. Energy Environ. Sci. *9*, 3120–3127. https://doi.org/10.1039/C6EE02017H.

33. Zheng, G., Su, X., Xie, H., Shu, Y., Liang, T., She, X., Liu, W., Yan, Y., Zhang, Q., Uher, C., et al. (2017). High thermoelectric performance of p-BiSbTe compounds prepared by ultra-fast thermally induced reaction. Energy Environ. Sci. *10*, 2638–2652. https://doi.org/10.1039/C7EE02677C.

34. Zhu, T., Fu, C., Xie, H., Liu, Y., and Zhao, X. (2015). High efficiency half-Heusler thermoelectric materials for energy harvesting. Adv. Energy Mater. *5*, 1500588. https://doi.org/10.1002/aenm.201500588.

35. Deng, R., Su, X., Hao, S., Zheng, Z., Zhang, M., Xie, H., Liu, W., Yan, Y., Wolverton, C., Uher, C., et al. (2018). High thermoelectric performance in Bi0.46Sb1.54Te3 nanostructured with ZnTe. Energy Environ. Sci. *11*, 1520–1535. https://doi.org/10.1039/C8EE00290H.

36. Bartholomé, K., Balke, B., Zuckermann, D., Köhne, M., Müller, M., Tarantik, K., and König, J. (2014). Thermoelectric modules based on half-Heusler materials produced in large quantities. J. Electron. Mater. *43*, 1775–1781. https://doi.org/10.1007/s11664-013-2863-x.

37. Hu, X., Yamamoto, A., and Nagase, K. (2015). Characterization of half-Heusler unicouple for thermoelectric conversion. J. Appl. Phys. *117*, 225102. https://doi.org/10.1063/1.4922127.

38. Liu, Z., Gao, W., Oshima, H., Nagase, K., Lee, C.-H., and Mori, T. (2022). Maximizing the performance of n-type Mg3Bi2 based materials for room-temperature power

generation and thermoelectric cooling. Nat. Commun. *13*, 1120. https://doi.org/10.1038/s41467-022-28798-4.

39. Li, W., Poudel, B., Nozariasbmarz, A., Sriramdas, R., Zhu, H., Kang, H.B., and Priya, S. (2020). Bismuth telluride/half-Heusler segmented thermoelectric unicouple modules provide 12% conversion efficiency. Adv. Energy Mater. *10*, 2001924. https://doi.org/10.1002/aenm.202001924.

40. Zhang, Q., Liao, J., Tang, Y., Gu, M., Ming, C., Qiu, P., Bai, S., Shi, X., Uher, C., and Chen, L. (2017). Realizing a thermoelectric conversion efficiency of 12% in bismuth telluride/skutterudite segmented modules through full-parameter optimization and energy-loss minimized integration. Energy Environ. Sci. *10*, 956–963. https://doi.org/10.1039/C7EE00447H.

41. Jiang, B., Yu, Y., Cui, J., Liu, X., Xie, L., Liao, J., Zhang, Q., Huang, Y., Ning, S., Jia, B., et al. (2021). High-entropy-stabilized chalcogenides with high thermoelectric performance. Science *371*, 830–834. https://doi.org/10.1126/science.abe1292.

42. Crane, D.T., Kossakovski, D., and Bell, L.E. (2009). Modeling the building blocks of a 10% efficient segmented thermoelectric power generator. J. Electron. Mater. *38*, 1382–1386. https://doi.org/10.1007/s11664-009-0673-y.

43. D'Angelo, J., Case, E.D., Matchanov, N., Wu, C.-I., Hogan, T.P., Barnard, J., Cauchy, C., Hendricks, T., and Kanatzidis, M.G. (2011). Electrical, thermal, and mechanical characterization of novel segmented-leg thermoelectric modules. J. Electron. Mater. *40*, 2051–2062. https://doi.org/10.1007/s11664-011-1717-7.

44. Snyder, G.J., and Snyder, A.H. (2017). Figure of merit ZT of a thermoelectric device defined from materials properties. Energy Environ. Sci. *10*, 2280–2283. https://doi.org/10.1039/C7EE02007D.

45. Demeke, W., Kim, Y., Jung, J., Chung, J., Ryu, B., and Ryu, S. (2022). Neural network-assisted optimization of segmented thermoelectric power generators using active learning based on a genetic optimization algorithm. Energy Rep. *8*, 6633–6644. https://doi.org/10.1016/j.egyr.2022.04.065.

46. Bu, Z., Zhang, X., Hu, Y., Chen, Z., Lin, S., Li, W., and Pei, Y. (2021). An over 10% module efficiency obtained using non-Bi2Te3 thermoelectric materials for recovering heat of <600 K. Energy Environ. Sci. *14*, 6506–6513. https://doi.org/10.1039/D1EE02253A.

47. Hsu, K.F., Loo, S., Guo, F., Chen, W., Dyck, J.S., Uher, C., Hogan, T., Polychroniadis, E.K., and Kanatzidis, M.G. (2004). Cubic AgPbmSbTe2+m: bulk thermoelectric materials with high figure of merit. Science *303*, 818–821. https://doi.org/10.1126/science.1092963.

48. Dresselhaus, M.S., Chen, G., Tang, M.Y., Yang, R.G., Lee, H., Wang, D.Z., Ren, Z.F., Fleurial, J.-P., and Gogna, P. (2007). New directions for low-dimensional thermoelectric materials. Adv. Mater. *19*, 1043–1053. https://doi.org/10.1002/adma.200600527.

49. Pei, Y., Shi, X., LaLonde, A., Wang, H., Chen, L., and Snyder, G.J. (2011). Convergence of electronic bands for high performance bulk thermoelectrics. Nature *473*, 66–69. https://doi.org/10.1038/nature09996.

50. Yamashita, O. (2001). Thermoelectric properties of heavily GaP- and P-doped Si0.95Ge0.05. J. Appl. Phys. *89*, 6241–6246. https://doi.org/10.1063/1.1352686.

51. Usenko, A.A., Moskovskikh, D.O., Gorshenkov, M.V., Korotitskiy, A.V., Kaloshkin, S.D., Voronin, A.I., and Khovaylo, V.V. (2015). Optimization of ball-milling process for preparation of Si–Ge nanostructured thermoelectric materials with a high figure of merit. Scripta Mater. *96*, 9–12. https://doi.org/10.1016/j.scriptamat.2014.10.001.

52. Yu, J., Fu, C., Liu, Y., Xia, K., Aydemir, U., Chasapis, T.C., Snyder, G.J., Zhao, X., and Zhu, T. (2018). Unique role of refractory Ta alloying in enhancing the figure of merit of NbFeSb thermoelectric materials. Adv. Energy Mater. *8*, 1701313. https://doi.org/10.1002/aenm.201701313.

53. Bathula, S., Jayasimhadri, M., Singh, N., Srivastava, A.K., Pulikkotil, J., Dhar, A., and Budhani, R.C. (2012). Enhanced thermoelectric figure-of-merit in spark plasma sintered nanostructured n-type SiGe alloys. Appl. Phys. Lett. *101*, 213902. https://doi.org/10.1063/1.4768297.

54. Zhao, L.D., Wu, H.J., Hao, S.Q., Wu, C.I., Zhou, X.Y., Biswas, K., He, J.Q., Hogan, T.P., Uher, C., Wolverton, C., et al. (2013). All-scale hierarchical thermoelectrics: MgTe in PbTe facilitates valence band convergence and suppresses bipolar thermal transport for high performance. Energy Environ. Sci. *6*, 3346. https://doi.org/10.1039/c3ee42187b.

55. Kang, H.B., Poudel, B., Li, W., Lee, H., Saparamadu, U., Nozariasbmarz, A., Kang, M.G., Gupta, A., Heremans, J.J., and Priya, S. (2020). Decoupled phononic-electronic transport in multi-phase n-type half-Heusler nanocomposites enabling efficient high temperature power generation. Mater. Today *36*, 63–72. https://doi.org/10.1016/j.mattod.2020.01.002.

56. Peng, K., Zhang, B., Wu, H., Cao, X., Li, A., Yang, D., Lu, X., Wang, G., Han, X., Uher, C., and Zhou, X. (2018). Ultra-high average figure of merit in synergistic band engineered Sn Na1−Se0.9S0.1 single crystals. Mater. Today *21*, 501–507. https://doi.org/10.1016/j.mattod.2017.11.005.

57. Meng, X., Liu, Z., Cui, B., Qin, D., Geng, H., Cai, W., Fu, L., He, J., Ren, Z., and Sui, J. (2017). Grain boundary engineering for achieving high thermoelectric performance in n-type skutterudites. Adv. Energy Mater. *7*, 1602582. https://doi.org/10.1002/aenm.201602582.

58. Wu, Y., Nan, P., Chen, Z., Zeng, Z., Lin, S., Zhang, X., Dong, H., Chen, Z., Gu, H., Li, W., et al. (2020). Manipulation of band degeneracy and lattice strain for extraordinary PbTe thermoelectrics. Research *2020*, 8151059–8151112. https://doi.org/10.34133/2020/8151059.

59. Zhao, W., Liu, Z., Sun, Z., Zhang, Q., Wei, P., Mu, X., Zhou, H., Li, C., Ma, S., He, D., et al. (2017). Superparamagnetic enhancement of thermoelectric performance. Nature *549*, 247–251. https://doi.org/10.1038/nature23667.

60. Hong, M., Chen, Z., Yang, L., Zou, Y., Dargusch, M.S., Wang, H., and Zou, J. (2018). Realizing zT of 2.3 in $Ge_{1-x-y}Sb_xIn_yTe$ via reducing the phase-transition temperature and introducing resonant energy doping. Adv. Mater. *30*, 1705942. https://doi.org/10.1002/adma.201705942.

61. Zheng, L., Zhang, X., Liu, H., Li, S., Zhou, Z., Lu, Q., Zhang, J., and Zhang, F. (2016). Optimized nanostructure and thermoelectric performances of Mg2(Si0.4Sn0.6)Sbx solid solutions by in situ nanophase generation. J. Alloys Compd. *671*, 452–457. https://doi.org/10.1016/j.jallcom.2016.02.057.

62. Zhang, S.n., Jiang, G.y., Zhu, T.j., Zhao, X.b., and Yang, S.h. (2011). Doping effect on thermoelectric properties of nonstoichiometric AgSbTe2 compounds. Int. J. Miner. Metall. Mater. *18*, 352–356. https://doi.org/10.1007/s12613-011-0446-5.

63. Zhang, F., Chen, C., Yao, H., Bai, F., Yin, L., Li, X., Li, S., Xue, W., Wang, Y., Cao, F., et al. (2020). High-performance N-type Mg3Sb2 towards thermoelectric application near room temperature. Adv. Funct. Mater. *30*, 1906143. https://doi.org/10.1002/adfm.201906143.

64. Lee, J.K., Park, S., Ryu, B., Lee, H.S., Park, J., and Park, S. (2021). Effect of defect interactions with interstitial Ag in the lattice of BixSb2−xTe3 alloys and their thermoelectric properties. Appl. Phys. Lett. *118*, 052102. https://doi.org/10.1063/5.0040808.

65. Wu, F., Song, H., Jia, J., and Hu, X. (2014). Thermoelectric properties of rare earth-doped n-type Bi2Se0.3Te2.7 nanocomposites. Bull. Mater. Sci. *37*, 1007–1012. https://doi.org/10.1007/s12034-014-0038-x.

66. Beltrán-Pitarch, B., Vidan, F., and García-Cañadas, J. (2021). Thermal contact resistance evaluation of a thermoelectric system by means of three I-V curves. Int. J. Heat Mass Tran. *173*, 121247. https://doi.org/10.1016/j.ijheatmasstransfer.2021.121247.

67. Beltrán-Pitarch, B., Vidan, F., and García-Cañadas, J. (2020). Characterization of thermal contacts between heat exchangers and a thermoelectric module by impedance spectroscopy. Appl. Therm. Eng. *165*, 114361. https://doi.org/10.1016/j.applthermaleng.2019.114361.

68. Lyeo, H.-K., and Cahill, D.G. (2006). Thermal conductance of interfaces between highly

dissimilar materials. Phys. Rev. B *73*, 144301. https://doi.org/10.1103/PhysRevB.73.144301.

69. Platzek, D., Karpinski, G., Stiewe, C., Ziolkowski, P., Drasar, C., and Muller, E. (2005). Potential-Seebeck-microprobe (PSM): measuring the spatial resolution of the Seebeck coefficient and the electric potential. In ICT 2005. 24th International Conference on Thermoelectrics, pp. 13–16. https://doi.org/10.1109/ICT.2005.1519875.

70. Bu, Z., Zhang, X., Shan, B., Tang, J., Liu, H., Chen, Z., Lin, S., Li, W., and Pei, Y. (2021). Realizing a 14% single-leg thermoelectric efficiency in GeTe alloys. Sci. Adv. *7*, eabf2738. https://doi.org/10.1126/sciadv.abf2738.

71. Camut, J., Ayachi, S., Castillo-Hernández, G., Park, S., Ryu, B., Park, S., Frank, A., Stiewe, C., Müller, E., and de Boor, J. (2021). Overcoming asymmetric contact resistances in Al-contacted Mg2(Si,Sn) thermoelectric legs. Materials *14*, 6774. https://doi.org/10.3390/ma14226774.

72. Chung, J., Ryu, B., and Park, S. (2020). Dimension reduction of thermoelectric properties using barycentric polynomial interpolation at Chebyshev nodes. Sci. Rep. *10*, 13456. https://doi.org/10.1038/s41598-020-70320-7.

73. Chung, J., Ryu, B., and Seo, H. (2022). Unique temperature distribution and explicit efficiency formula for one-dimensional thermoelectric generators under constant Seebeck coefficients. Nonlinear Anal. R. World Appl. *68*, 103649. https://doi.org/10.1016/j.nonrwa.2022.103649.

STAR★METHODS

KEY RESOURCES TABLE

REAGENT or RESOURCE	SOURCE	IDENTIFIER
Deposited data		
Thermoelectric property database: Starrydata2.org, rawdata 20211124.zip	Starrydata2.org; GitHub	https://github.com/starrydata/starrydata_datasets/tree/master/datasets
(**data010**) Sample's formatted thermoelectric properties.	This paper; Mendeley Data	https://doi.org/10.17632/r9bhpv6vx9.1
(**data030**) Sample information and metadata table	This paper; Mendeley Data	https://doi.org/10.17632/r9bhpv6vx9.1
(**data040**) Sample's filtering table	This paper; Mendeley Data	https://doi.org/10.17632/r9bhpv6vx9.1
(**data070**) Sample's interpolated TEPs	This paper; Mendeley Data	https://doi.org/10.17632/r9bhpv6vx9.1
(**data150**) Sample's composition classification into material group	This paper; Mendeley Data	https://doi.org/10.17632/r9bhpv6vx9.1
(**data234**) Material efficiency raw data for different interfaces	This paper; Mendeley Data	https://doi.org/10.17632/r9bhpv6vx9.1
(**data261**) Material efficiency raw data (only for 25 K interpolated)	This paper; Mendeley Data	https://doi.org/10.17632/r9bhpv6vx9.1
(**data300**) Device configuration data generated using high-efficiency P- and N-samples	This paper; Mendeley Data	https://doi.org/10.17632/r9bhpv6vx9.1
(**data400**) Device efficiency data (only for optimal currents, small-size version)	This paper; Mendeley Data	https://doi.org/10.17632/r9bhpv6vx9.1
(**data500**) Best *ZT*s, best material and device efficiencies from calculations, and experimentally reported efficiencies	This paper; Mendeley Data	https://doi.org/10.17632/r9bhpv6vx9.1
(**data600**) 9 representative best efficiency P-N leg-pair devices	This paper; Mendeley Data	https://doi.org/10.17632/r9bhpv6vx9.1
(**data700**) A multiple-stage P-N leg pair device with a very high efficiency of 23.9%	This paper; Mendeley Data	https://doi.org/10.17632/r9bhpv6vx9.1
Software and algorithms		
Python 3.8. 5	Python software foundation	https://www.python.org
NumPy 1.19.2	NumPy project and community	http://www.numpy.org/
SciPy 1.5.2	SciPy developers	https://scipy.org/
Pandas 1.1.3	Pandas developers	https://pandas.pydata.org/
Barycentric polynomial interpolation at Chebyshev nodes	Chung et al.[72]	https://doi.org/10.1038/s41598-020-70320-7
One-dimensional temperature-solving integral algorithm for a thermoelectric leg	Ryu et al.[15]	https://doi.org/10.1016/j.isci.2021.102934

RESOURCE AVAILABILITY

Lead contact

- Further information and requests for resources should be directed to and will be fulfilled by the lead contact, Byungki Ryu (byungkiru@keri.re.kr).

Materials availability

- This study did not generate new unique reagents.

Data and code availability

- Data for the thermoelectric properties, related sample and publication information, and calculated efficiencies have been deposited at Mendeley and are publicly available as of the date of publication (Mendeley Data: https://doi.org/10.17632/r9bhpv6vx9.1), as summarised in the key resources table. The DATAIDs and related calculation processes are described in the STAR Methods (overview of efficiency calculation process).
- This paper does not report original code. Instead, all detailed algorithms are explained in the STAR Methods.

- Any additional information required to reanalyse the data reported in this paper is available from the lead contact upon request.

EXPERIMENTAL MODEL AND SUBJECT DETAILS

This study did not perform experimental works. This study is theoretical.

METHOD DETAILS

Overview of efficiency calculation process

The best thermoelectric efficiency is calculated and explored using the following procedure. The values in parentheses at the end of the following sentences are the corresponding data identification codes (**DATAID**s) for the analysis and data. First, a formatted thermoelectric property file (**data010**) is generated by extracting the raw data from **Starrydata2**. A sample metadata file (**data030**) is also generated; it contains thermoelectric data length, data reference, composition information, available temperature range, published date, etc. A data filter is used to test that each material sample's dataset of thermoelectric properties is complete, valid, or errorless, and the result is recorded as sample lists (**data040**). The thermoelectric properties are interpolated (**data070**) for the *ZT* distribution analysis. Composition data are transformed into a composition vector, and the samples are classified into given material groups (**data150**). The thermoelectric material efficiency of the samples in the list is computed for available temperature ranges (**data234**), and material efficiency data are interpolated (**data261**). Using high-efficiency samples, P-N leg pair device configurations are generated (**data300**), and the device efficiencies are computed (**data400**). Finally, the best *ZT*, best material efficiency, and best device efficiency curves are obtained (**data500**). The best efficiencies are compared to the experimentally reported device efficiencies (**data500**). Among them, 9 representative best efficiency devices are analysed (**data600**). A multiple-stage P-N leg pair device with a very high efficiency of 23.9% is found (**data700**). Related data of corresponding **DATAID**s have been deposited at Mendeley and are publicly available as of the date of publication (Mendeley Data: https://doi.org/10.17632/r9bhpv6vx9.1) as summarized in the key resources table.

Data preparation, filtering, and cleansing

High-quality thermoelectric property data are obtained from the **Starrydata2** thermoelectric web-DB,[17] which is growing with time. For the investigations, we use the thermoelectric property data of version 2021-November-24, consisting of 43,601 material samples from 7,994 published papers ("20211124.zip" in https://github.com/starrydata/starrydata_datasets). Among them, 16,420 samples are chosen from 3,585 published papers that contain a full set of three thermoelectric properties. Note that a *complete* set of thermoelectric properties is mandatory for the calculation of thermoelectric performance. Then, high-quality thermoelectric property data are obtained after filtering out unphysical and erroneous data. A total of 33 data filters are used, that is, *physics filters* to remove unphysical values of thermoelectric properties and temperature ranges and *error filters* to remove insufficiently/incorrectly labelled data that are hardly readable by a computer. See key resources table (**data040**) for the thermoelectric sample filtering table. For high-efficiency samples, the correctness of the thermoelectric properties from **Starrydata2** is confirmed by visual inspection. Consequently, high-quality thermoelectric property data are obtained, which consist of 13,338 complete and valid samples from 3,120 published papers. The corresponding data size is 215,526 $(T, \alpha(T))$ pairs, 223,404 $(T, \rho(T))$ pairs, and 187,244 $(T, \kappa(T))$ pairs. For efficiency calculations, thermoelectric properties are interpolated in a piecewise linear manner and extrapolated in a constant value manner so that the resulting properties are continuous functions of temperature. Among the complete and valid samples, 12,645 samples from 2,919 publications have thermoelectric properties at $T_h > 300$ K. Using these samples, thermoelectric efficiencies at $T_h > 300$ K are evaluated for various device models: see key resources table (**data261**). Related data on the corresponding **DATAID**s have been deposited at Mendeley and are publicly available as of the date of publication (Mendeley Data: https://doi.org/10.17632/r9bhpv6vx9.1) as summarized in the key resources table.

Thermoelectric device model

In the thermoelectric device, P- and/or N-type thermoelectric materials, called thermoelectric legs, are placed between hot- and cold-side substrates. The thermal boundary conditions are assumed to be the Dirichlet condition, which means that T_h and T_c are fixed during device operation. We compute the theoretical maximum conversion efficiency, ignoring radiation and convection losses. The length of a thermoelectric leg is assumed to be 3 mm. Since the leg is connected to substrates, we consider the interfacial

electrical and thermal resistances. The electrical and thermal resistances are simultaneously imposed using two additional segments of 0.1 mm attached at the ends of the leg unless interfacial resistances are zero; in total, the leg length is 3 mm for a perfect interface and 3.2 mm if there are interfacial resistances. We assume that the electrical and thermal currents flow perpendicular to the substrate, which implies a one-dimensional flow. For a single-leg device, the leg cross-sectional area of $A = 3\,\text{mm} \times 3\,\text{mm}$ is adopted. For a P-N leg-pair device, the cross-sectional areas of P- and N-type legs (A_p, A_n) are set to $A_p = (1-x)\cdot A$ and $A_n = x\cdot A$, for a number x between 0.02 and 0.98. For x, we consider 11 values at the Chebyshev nodes of the second kind[72] between 0.02 and 0.98.

Thermoelectric performance calculation

In a one-dimensional thermoelectric leg, the heat currents at the hot and cold sides (Q_h, Q_c) and the power P are given as follows:

$$Q_{h,c} = -A\kappa_{h,c}\left(\frac{dT}{dx}\right)_{h,c} + I\,\alpha(T_{h,c})T_{h,c}, \qquad \text{(Equation 4)}$$

$$P = Q_h - Q_c, \qquad \text{(Equation 5)}$$

where h and c denote the hot and cold sides, A is the leg cross-sectional area, and I is the electric current flowing through the leg. Once the temperature distribution inside the leg is known, the thermoelectric material efficiency can be easily computed for given electrical and thermal conditions:

$$\eta^{(\text{mat})} = \eta(I, T_h, T_c) = \frac{Q_h - Q_c}{Q_h}. \qquad \text{(Equation 6)}$$

The P-N leg-pair device efficiency can be computed as follows:

$$\eta^{(\text{dev})} = \frac{P^{(\text{tot})}}{Q_h^{(\text{tot})}} = \frac{P^{(p)} + P^{(n)}}{Q_h^{(p)} + Q_h^{(n)}}. \qquad \text{(Equation 7)}$$

Temperature distribution inside a leg

In a steady-state one-dimensional leg, thermoelectric effects are governed by the following thermoelectric differential equation[15,73]:

$$\frac{d}{dx}\left(\kappa\frac{dT}{dx}\right) - T\left(\frac{d\alpha}{dT}\right)\left(\frac{dT}{dx}\right)J + \rho J^2 = 0. \qquad \text{(Equation 8)}$$

This equation can be transformed into a thermoelectric integral equation for temperature distribution $T(x)$ via double integration on $f_T(x) := -T\frac{d\alpha}{dT}\frac{dT}{dx}J + \rho J^2$ as follows[15]:

$$T(x) = \left(T_h - \frac{K\Delta T}{A}\int_0^x \frac{1}{\kappa(s)}ds\right) + \left(-\int_0^x \frac{F_T(s)}{\kappa(s)}ds + \frac{K\delta T}{A}\int_0^x \frac{1}{\kappa(s)}ds\right), \qquad \text{(Equation 9)}$$

where $F_T(x) := \int_0^x f_T(s)ds$, $\delta T := \int_0^L \frac{F_T(x)}{\kappa(x)}dx$, and L is the leg length. By iteratively computing (9), we find the temperature distribution inside the legs.[15]

Computation of the best efficiency

A thermoelectric sample is evaluated using the maximum thermoelectric efficiency calculation under various temperature differences $\Delta T = T_h - T_c$, where the cold-side temperature is 300 K and T_h is chosen between 301 K and the maximum available temperature ($T_{\max}$) plus 15 K, including two ends. For T_h, we consider 11 values at the Chebyshev nodes of the second kind[72] between 301 K and T_h.

The generated electrical power and input heat current are computed using Equations 4, 5, 6, 7, 8, and 9 [15] under a given electrical current and thermal boundary conditions. Then, the maximum efficiencies are searched by varying electrical currents for 12,645 samples, which are available for T > 300 K. Using the searched high-performance P- and N-samples, of which the efficiency is larger than or equal to 85% of the best efficiency, single-stage P-N leg-pair configurations of 14,702 are constructed; see key resources

table (**data300**). We also consider 11 leg-pair geometries and 5 interfacial resistance conditions for the P-N leg-pair devices. In total, 63,225 (= 12,645 ×1 ×5) single-leg devices and 808,610 (= 14,702 ×11 ×5) P-N leg-pair devices are considered. For each device configuration, 11 electrical current points and 11 thermal boundary conditions are considered. During this process, the leg geometry parameter x, current I, and temperature T_h are sampled at the Chebyshev node of the second kind, which is suited for polynomial interpolation.[72] In total, we calculate $\eta^{(mat)}$'s for 7,650,225 configurations (over 12645 materials, 5 interfaces, 11 I points, 11 T_h points) and $\eta^{(dev)}$'s for 97,841,810 configurations (over 14702 material leg pairs, 11 geometry x values, 5 interfaces, 11 I points, 11 T_h points). Finally, we explore the 100 million thermoelectric material and device efficiency space (7650225 material cases + 97841810 device cases = 105,492,035 efficiencies) and obtain the best thermoelectric efficiencies.

Dimensional effect and radiation loss

We tested the efficiency performance difference between the one- and three-dimensional models. For three-dimensional leg-pair calculations, the efficiencies are found to be dependent on leg geometry. The efficiency difference between the 3 mm×3 mm×3 mm leg and 0.5 mm×0.5 mm×3 mm was found to be −3.6%. As the ratio of leg height to leg width increases, the efficiency increases and converges to 1-dimensional leg efficiency. Adding radiation (RAD) and convection (CONV) heat transfers from the device to the outside may lower thermoelectric efficiency. Thus, we can conclude that the one-dimensional model gives the upper bound for the best thermoelectric efficiency:

$$\eta^{(1-\mathrm{dim})} \geq \eta^{(3-\mathrm{dim})} \geq \eta^{(3-\mathrm{dim})+(\mathrm{RAD\ and\ CONV})}.$$

Depending on the geometry and heat source temperature, the thermoelectric efficiency can be further reduced by ∼20% or more,[19] when blackbody-like radiation occurs, that is, the emissivity is 1.

Material group classification of compositions

Samples are grouped into 17 material groups based on composition analysis. We manually define the 17 material groups with representative compositions. To classify a sample into a material group, the fraction of host or anionic elements is calculated. If the fraction is greater than a certain value (90% for the host, 30% for anionic analysis, 20% for oxide classification), then the sample is grouped into one of the 17 material groups of which the representative composition is most similar to the sample's composition. For example, $(Bsi_{0.4}Sb_{1.6})Te_3Ag_{0.03}$ is similar to $Bi_2Te_3Ag_{0.03}$ and is grouped into Bi_2Te_3. The classification results can be found in the key resources table (**data150** and **data261**).

ADDITIONAL RESOURCES

There are two related preprint versions of this paper by same authors.

- At arXiv.org: https://doi.org/10.48550/arXiv.2210.08837.
- At Research Square: https://doi.org/10.21203/rs.3.rs-2179853/v1.